Volcanic precursor revealed by machine learning offers new eruption forecasting capability

Kaiwen Wang[1], Felix Waldhauser[1], Maya Tolstoy[1,2], David Schaff[1], Theresa Sawi[1], William Wilcock[2], Yen Joe Tan[3]

[1]Lamont-Doherty Earth Observatory, Columbia University
[2]School of Oceanography, University of Washington
[3]Earth and Environmental Sciences Programme, The Chinese University of Hong Kong

Key Points:

- Unsupervised learning separated regular earthquakes and precursory mixed frequency earthquakes (MFEs) based on different spectral patterns
- The regular earthquakes have strong tidal modulation, corresponding to failures on the caldera ring faults triggered by tidal stress changes
- The MFEs emerge 15 hours before eruption and migrate along pre-existing fissures, likely associated with eruption preparation processes

Corresponding author: Kaiwen Wang, kw2988@columbia.edu

Abstract

Seismicity at active volcanoes provides crucial constraints on the dynamics of magma systems and complex fault activation processes preceding and during an eruption. We characterize time-dependent spectral features of volcanic earthquakes at Axial Seamount with unsupervised machine learning methods, revealing mixed frequency signals that emerge from the continuous waveforms about 15 hours before eruption onset. The events migrate along pre-existing fissures, suggesting that they represent brittle crack opening driven by influx of magma or volatiles. These results demonstrate the power of novel machine learning algorithms to characterize subtle changes in magmatic processes associated with eruption preparation, offering new possibilities for forecasting Axial's anticipated next eruption. This novel method is generalizable and can be employed to identify similar precursory signals at other active volcanoes.

Plain Language Summary

Our research used observations of small earthquakes to understand the dynamic behaviors of magma and fault systems before and during a volcano eruption. Specifically, we used machine learning techniques to search for signature waveform patterns that may inform us of their associated physical processes. At Axial Seamount, an active underwater volcano, we discovered distinct patterns in earthquake signals preceding and during the 2015 eruption. Based on event spectral patterns, we identified signals of mixed-frequency earthquakes that emerge about 15 hours before the eruption starts and migrate along pre-existing eruptive fissures. The spectral pattern involves a mixture of low frequency energy following the first arrivals, which we interpret to represent opening of cracks and being filled with magma or gases. Our study demonstrates that we can use machine learning algorithms to detect subtle changes in volcanic signals and help us better understand the processes leading up to an eruption. This may help us in forecasting Axial's upcoming eruption and can possibly be applied to other active volcanoes too.

1 Introduction

Seismic observations can provide important constraints on the structure of a volcano and its dynamic behavior in volcanic cycles (Wilcock et al., 2016; Wilding et al., 2023; Tan et al., 2019; Gudmundsson et al., 2016). Questions remain on how magma moves in the subsurface preceding an eruption and how soon before an eruption this process begins. Recent advances in unsupervised machine learning methods (Holtzman et al., 2018; Cotton & Ellis, 2011; Holtzman et al., 2021; Sawi et al., 2022; Yoon et al., 2015; Seydoux et al., 2020; Jenkins et al., 2021) offer the opportunity to mine large waveform archives to find subtle differences in the spectral content of seismic signals. These differences can be interpreted with respect to changes in source characteristics and the volcano-tectonic processes that drive brittle failure, providing a time-dependent image of physical processes that lead up to an eruption.

Axial Seamount is a well-instrumented, active submarine volcano on the Juan de Fuca Ridge (Figure 1) with a long record of geophysical data that covers the last three eruptions in 1998, 2011, and 2015 (Wilcock et al., 2018, 2016; Nooner & Chadwick, 2016), including documentation of the eruptive fissures and lava flows of the recent 2015 eruption (Chadwick et al., 2016), and 3-D images of its shallow magma chamber (Arnulf et al., 2014). Five months before the most recent eruption in April 2015, seismicity at Axial Seamount has been recorded by a local, cabled, 7-station ocean bottom seismometer (OBS) network operated in real-time by the Ocean Observatories Initiative (OOI) (Kelley et al., 2014). The OBS array recorded signals from a variety of sources (Wilcock et al., 2016). Here we apply unsupervised machine learning methods to the 4 months before and during the 2015 eruption to find precursory signals with distinct frequency content.

2 Supervised and Unsupervised ML

We combined supervised machine learning (ML) techniques (Zhu & Beroza, 2019; Zhu et al., 2022) with cross-correlation-based, high-resolution earthquake relative location methods (Waldhauser & Ellsworth, 2000; Waldhauser et al., 2020; Lomax et al., 2000, 2009) to develop a catalog of 240,000 earthquakes (M = -1.74 to 3.45) for Axial Seamount from 2014 to 2021. The new earthquake catalog illuminates the caldera ring faults and the fissures that were active during the previous eruptions (Figure 1) (Wilcock et al., 2016; Waldhauser et al., 2020).

We then apply an unsupervised machine learning method (SpecUFEx, Holtzman et al., 2018) to the 4 months of pre-eruption data to characterize spectral patterns in the waveforms. SpecUFEx is an unsupervised spectral feature extraction algorithm originally developed using ML methods for audio pattern recognition (Cotton & Ellis, 2011)

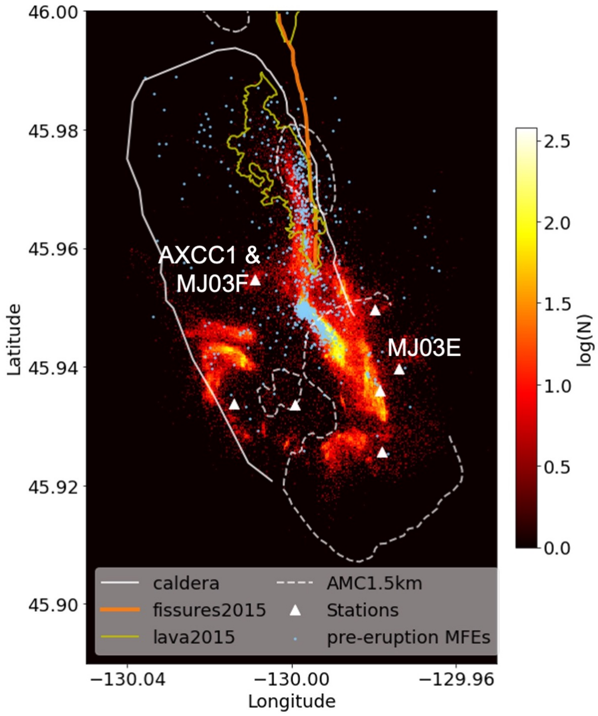

Figure 1. Heatmap of earthquake density at Axial Seamount from Nov 2014 to Dec 2021. Mixed-frequency earthquakes (MFEs) one day before the eruption are shown in light blue dots. Also shown are the caldera rim (white solid line), the 1.5 km depth contour of the Axial magma chamber (AMC) (dashed white line), eruptive fissures (orange lines), and lava flows (yellow lines) of the 2015 eruption and the OBS array (white triangles). The heatmap shows the number of earthquakes in each bin (bin size 25m × 25m).

and has been later adapted to characterize seismic waveforms of earthquakes (Holtzman et al., 2018), acoustic emissions (Holtzman et al., 2021), icequakes (Sawi et al., 2022), and repeating earthquakes (Sawi et al., 2023). It takes event spectrograms as input and applies nonnegative matrix factorization (NMF) and hidden Markov models (HMM) to reduce the dimensionality of the spectral features and remove features that are common to all signals. For each earthquake, we calculate a fingerprint matrix by counting the number of state transitions in the state sequence matrix from the HMM output. The fingerprints are condensed representations of the original earthquake spectrograms while still keeping their time-dependent spectral information. We further compress the fingerprints by principal component analysis (PCA) and finally apply K-means clustering to identify earthquake clusters that have common spectral features (Holtzman et al., 2018). We focus our analysis on the 4 months of seismicity leading up to the eruption on April 24,

2015. We use waveform data from broadband OBS station AXCC1 and learned the feature dictionary on a representative subset of ∼9,000 events in the week before the eruption. We then use the learned dictionary to calculate features of the ∼4 months of seismicity starting from the beginning of 2015 until the eruption onset.

3 Spectral differences

K-means clustering of the fingerprints separates the events into two main groups with small but distinct differences in spectral features in the waveforms between the groups (Figure 2A and 2D). To investigate which characteristic spectral features might contribute to the separation of the two earthquake clusters, we examine the representative patterns of the condensed fingerprints. By stacking the top 100 representative fingerprints in each cluster (Figure 2B and 2E), we identify the active states (bright spots in stacked fingerprints). These active states are the characteristic features that define the spectral feature space. We project these characteristic features in the fingerprints back onto the HMM and NMF mappings (emissions matrix in Figure S3A and spectral dictionary in Figure S3B) to solve for their frequency-dependent sensitivity kernel (Figure S3C). Comparing the frequency dependency of the characteristic features in the two clusters, we find that one cluster has events with lower frequency content coming in shortly (∼1 s) after the P-arrival. Thus we define the earthquakes in this cluster as mixed-frequency earthquakes (MFEs) and the events in the other cluster as regular earthquakes (EQs). The spectral differences can also be seen in the stacked spectrograms (Figure 2C and 2F) of the top 100 representative events and their waveforms (Figure 2A and 2D).

4 Spatio-temporal distribution

The separation based on spectral characteristics reveals differences in the spatiotemporal evolution of the earthquakes in the two groups (Figure 3, Movie S1). Approximately 24 hours prior to the eruption, the MFEs start lighting up the eastern margin of the caldera along the southern segment of the eruptive fissures (Figure 1). These MFEs locate close to the roof of the Axial magma chamber (∼1.5 km; 15). ∼15 hours before the eruption, a distinct burst of MFEs migrates from the caldera center northward along the eastern margin of the caldera at a speed of 4.4 km/h (arrow in Figure 3B). The peak hourly moment release of the MFEs during that burst is about two orders of magnitude above background, and 40 times that released by all regular earthquakes in the same period. Af-

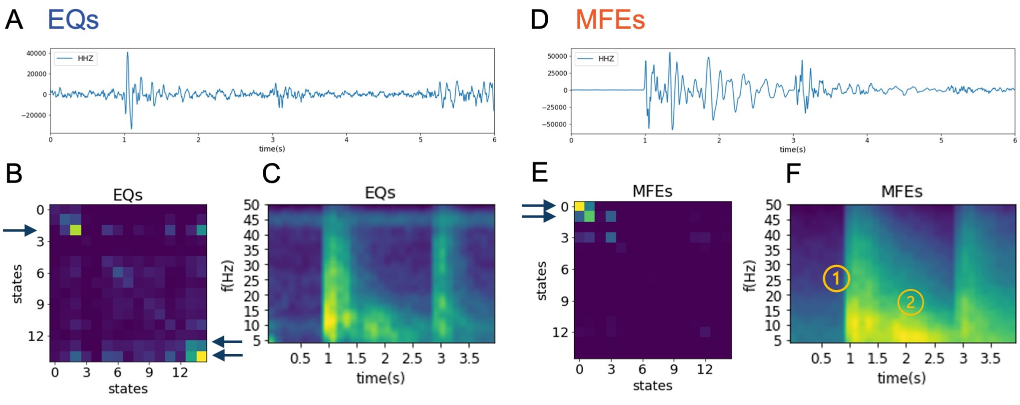

Figure 2. Spectral characteristics of events in the two main clusters. Waveform examples of one representative event in each cluster (A and D), stacked fingerprints (B and E), and stacked spectrograms (C and F) using 100 events in each cluster. The stacked fingerprints and stacked spectrograms are color scaled by their maximum value. ① and ② in F mark the impulsive P arrival and the low-frequency tail.

ter this initial burst, the MFE activity subsides for a couple of hours and then, about 3.5 hours before the eruption, a second burst of MFEs occurred, reversing the path of the previous burst and migrating southward (at a speed of 1.1 km/hr) and eventually upward towards the location where the lava first erupted on the seafloor (Wilcock et al., 2016) (Figure 3B). After that point and for the next hour, the MFEs spread out across the entire fault system during the course of the eruption. The second MFE burst is characterized by a steep increase in seismic moment release starting about 4 hours and peaking 1 hour before the eruption onset. Peak hourly moment release is about 30 times that of the first burst, while the moment release from regular earthquakes leading up to the eruption is comparably insignificant. Once the eruption starts, MFE moment release continuously decreases, while that from regular earthquakes increases.

Different from the MFEs, the regular earthquakes locate primarily in the southern part of the caldera (Figure S5). They occur on both the eastern and western walls of the ring fault, which suggests that the spectral fingerprints are not sensitive to event location relative to the seismic station. The regular earthquake cluster also includes events during the pre-eruption inflation period as well as the rapid deflation period after the eruption started, that is, when the fault slip motion on the caldera ring faults reversed

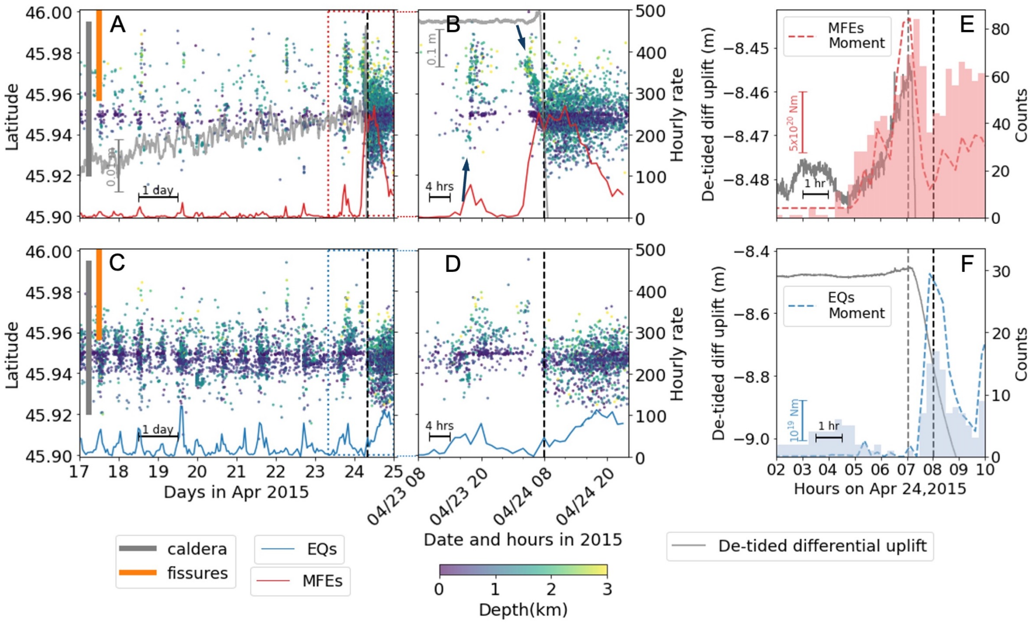

Figure 3. Pre-eruption temporal evolution of the two spectral clusters. The MFEs (top panels) and earthquakes (bottom panels) spatiotemporal distribution in ∼1 week (A and C), ∼2 days (B and D), and 8 hours (E and F) time scale. The top and bottom panels are plotted with the same time axis for MFEs (A, B, and E) and earthquakes (C, D, and F) activity. The red and blue curves (A - D) are hourly seismicity rates. Grey curves (A - F) show volcano inflation represented by detided differential uplift measurement between two bottom pressure recorders (BPRs) at sites MJ03E and MJ03F (Figure 1)(Chadwick et al., 2022). Dashed red and blue curves (E and F) show the binned seismic moment of the MFEs and earthquakes during the eruption. The dashed black vertical line (A - F) marks the time of eruption onset at 8:01 when the lava first reaches the seafloor(Wilcock et al., 2016). Arrows in (B) point to northward and southward migration prior to the eruption. The dashed gray vertical line (E and F) marks the time of maximum inflation at 7:03 (E and F).

from normal faulting to thrust faulting (Wilcock et al., 2016). This suggests that the fingerprints are also not sensitive to the reversal of fault slip motion.

Tidal triggering of earthquakes is observed at Axial seamount, especially prior to the eruption (Wilcock et al., 2016; Scholz et al., 2019; Tan et al., 2019; Tolstoy et al., 2002). Here, we compare the temporal correlation between the two spectral clusters we identified and the ocean tide to understand their driving mechanisms. We find that the rate of regular earthquakes closely follows the tidal cycle over the observation period (Figure 3D, Figure S6). Given their locations and the temporal correlation with the tides, we infer that these earthquakes generally occur on critically stressed ring faults and are triggered by small stress changes. The MFE cluster, during the same period, shows rather sparsely distributed bursts of events (Figure S4A) which mostly lie along the eastern edge of the caldera to the north (Figure S7). Among these bursts, we do not observe a clear migration pattern over long distances (Figure S7) as seen in the two very active bursts that relate to the north-south migration $\sim$15 hours and $\sim$3.5 hours before the eruption onset (Figure 3B). The timings of the MFE bursts correlate with the tides in many cases (Figure S4), but they locate further to the north compared with the tidal driven earthquakes (Figure 3). We do not observe systematic offset between the timing of the MFE bursts and the peak of regular earthquakes. This suggests that the underlying driver for the two different types of earthquakes may be the same (e.g., magma pressure), or that the drivers respond to the tidal forcing in a similar way.

5 Possible mechanisms

Two possible explanations of the spectral feature difference are path effect and source effect. Spatially variant attenuation patterns, especially in local complex volcanic structures, may cause differences in frequency content if observed along different paths. However, we find that the same clustering analysis carried out at other stations (AXAS1, AXEC2) in the OBS network gives similar groupings (Supplementary materials, Figure S2). If path effects were causing the clustering, we would expect different event groupings at stations that sample different source-receiver paths. It is also possible that attenuation or velocity changes occur in a region that is local to the source. However, we find that closely located and timed events from the two groups still show different spectral behavior at a common station. Therefore, we infer that the spectral difference between the two groups is likely caused by differences in the source mechanisms.

There are many possibilities that can explain source differences, including differences in fault stress state, faulting mechanisms, or the effects of fluid. Wilcock et al. (2016) detected southward migration of pre-eruption seismicity along the east wall in the hours before the eruption and associated it with southward dike propagation and opening of eruptive fissures. It is possible that the MFEs are tracking magma flows into the opening cracks and thus include non-double-couple components from the crack opening mode in contrast to simple shear failures of earthquakes on the ring faults (Foulger et al., 2004). In this process, the low-frequency content in the MFE waveforms might be generated by magma or volatiles filling the crack, as observed in studies at other regions (Chouet & Matoza, 2013; Cui et al., 2021; Woods et al., 2018; Song et al., 2023).

When comparing the moment release of MFEs with available differential elevation data (Nooner & Chadwick, 2016) we find that the peak moment coincides with the peak in inflation about one hour before the eruption (Figure 3H). Moment release for the earthquakes, on the other hand, is highest during the time of rapid deflation after lava erupted. This suggests the MFEs are associated with magmatic processes during the pre-eruption inflation process, while the regular earthquakes are triggered by the stress change on the ring faults as the magma chamber deflates. In the pre-eruption period, the MFEs in the north also correlate with the region of maximum uplift observed in deformation measurement (Nooner & Chadwick, 2016), illuminating the segment of the eruptive fissure where the following eruption started.

Given that the MFEs locate along the eruptive fissures near the roof of the magma chamber and the documented high CO2 content at the Axial seamount (Dixon et al., 1988), the MFEs are likely caused by brittle crack opening and subsequent movement of magma and/or volatiles into the zones of weakness created by increasing magma pressure. In fact, the observation that they distribute widely in space and time suggests they are more likely related to CO2 release as opposed to magma movement. Because MFEs are detected for months prior to the eruption, it implies there is an extended period of magma intrusion or volatile release possibly associated with inflating sills. However, the behavior of early MFE bursts suggests that this magmatic process may occur at a small scale at depth so that they do not show a clear migration pattern along the dike, consistent with the presence of volatiles. As the magma pressure builds up, the dike finally forms along the weakened zones and initiates the southward propagation, which is observed as intense MFE activity starting ∼3.5 hours before the eruption. Figure 4 shows a cartoon summarizing the physical processes and associated seismicity at Axial.

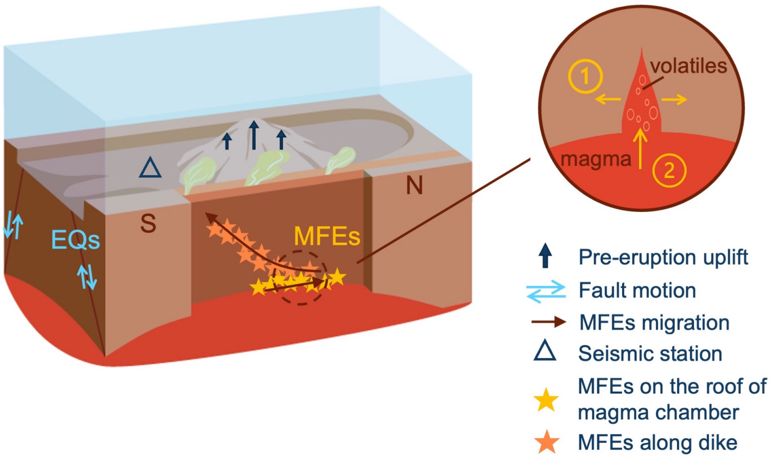

Figure 4. Cartoon summarizing observations. Tidal-driven earthquakes occur on caldera ring faults while the MFEs track movement of volatiles and magma prior to the eruption. Inset shows possible mechanisms of the MFEs. ① and ② correspond to the crack opening (brittle onset in Figure 2F) and volatile/magma influx (low-frequency tail in Figure 2F) processes.

Short-term volcano eruption forecasting has long been a challenging task due to the lack of clear and reliable precursory signals. Common prediction metrics include long-term deformation measurement, changes in tidal triggering, and short-term seismicity increase (Wilcock et al., 2018, 2016; Nooner & Chadwick, 2016). In this study, unsupervised ML revealed the emergence of a precursory signal defined as MFEs. These signals differ substantially from volcano-tectonic (VT; White and McCausland (2016)) or long-period (LP; Woods et al. (2018); Song et al. (2023)) earthquakes or tremors (Dempsey et al., 2020), as they contain both short and long period waves. Although they may resemble some of the previously reported hybrid frequency earthquakes (HFE; Harrington and Brodsky (2007); Yu et al. (2021); Coté et al. (2010); Cui et al. (2021)), our observations suggest that their mechanism might be different. Interpretations of previously observed hybrid earthquakes include path effects caused by strong attenuation or low-velocity layers, and source effects due to low stress drop, slow rupture speed, or fluid resonance. Our analysis indicates that the characteristic spectral features of the MFEs likely originate from source effects rather than path effects, making them a potential precursory signal to track magma movement or volatile release at depth. This precursory MFE activity intensifies ∼15 hours before the eruption and peaks ∼1 hour before the magma reaches the seafloor, which offers an opportunity to improve short-term eruption forecasting on time scales of hours to days. With the capability to identify such precursory signal in real time, we can now monitor these signals as Axial is preparing for its next eruption to occur within the 2025-2030 time period (Chadwick et al., 2022). More importantly, the novel use of unsupervised machine learning opens up a new opportunity to investigate whether such precursory seismic signals exist at other active volcanoes.

Data Availability Statement

Seismic waveforms used in this study were downloaded from the Incorporated Research Institutions for Seismology (IRIS) Data Management Center (DMC) (`https://ds.iris.edu/ds/nodes/dmc/data/`). The earthquake catalog is available on Figshare (`https://figshare.com/s/1cf6c6dadfa6cdefdbb1`).

Acknowledgments

This work received support from NSF awards OAC-2103741 and NSF OCE-1951448. We would like to thank anonymous reviewers for providing constructive comments and suggestions to improve the manuscript.

References

Arnulf, A., Harding, A., Kent, G., Carbotte, S., Canales, J., & Nedimović, M. (2014). Anatomy of an active submarine volcano. *Geology*, *42*(8), 655–658.

Baillard, C., Wilcock, W. S., Arnulf, A. F., Tolstoy, M., & Waldhauser, F. (2019). A joint inversion for three-dimensional p and s wave velocity structure and earthquake locations beneath axial seamount. *Journal of Geophysical Research: Solid Earth*, *124*(12), 12997–13020.

Chadwick, W., Paduan, J., Clague, D., Dreyer, B., Merle, S., Bobbitt, A., . . . Nooner, S. (2016). Voluminous eruption from a zoned magma body after an increase in supply rate at axial seamount. *Geophysical Research Letters*, *43*(23), 12–063.

Chadwick, W., Wilcock, W. S., Nooner, S. L., Beeson, J. W., Sawyer, A. M., & Lau, T.-K. (2022). Geodetic monitoring at axial seamount since its 2015 eruption reveals a waning magma supply and tightly linked rates of deformation and seismicity. *Geochemistry, Geophysics, Geosystems*, *23*(1), e2021GC010153.

Chouet, B. A., & Matoza, R. S. (2013). A multi-decadal view of seismic methods for detecting precursors of magma movement and eruption. *Journal of Volcanology and Geothermal Research*, *252*, 108–175.

Coté, D. M., Belachew, M., Quillen, A. C., Ebinger, C. J., Keir, D., Ayele, A., & Wright, T. (2010). Low-frequency hybrid earthquakes near a magma chamber in afar: quantifying path effects. *Bulletin of the Seismological Society of America*, *100*(5A), 1892–1903.

Cotton, C. V., & Ellis, D. P. (2011). Spectral vs. spectro-temporal features for acoustic event detection. In *2011 ieee workshop on applications of signal processing to audio and acoustics (waspaa)* (pp. 69–72).

Cui, X., Li, Z., & Huang, H. (2021). Subdivision of seismicity beneath the summit region of kilauea volcano: Implications for the preparation process of the 2018 eruption. *Geophysical Research Letters*, *48*(20), e2021GL094698.

Dempsey, D., Cronin, S. J., Mei, S., & Kempa-Liehr, A. W. (2020). Automatic precursor recognition and real-time forecasting of sudden explosive volcanic eruptions at whakaari, new zealand. *Nature communications*, *11*(1), 3562.

Dixon, J. E., Stolper, E., & Delaney, J. R. (1988). Infrared spectroscopic measurements of co2 and h2o in juan de fuca ridge basaltic glasses. *Earth and Planetary Science Letters*, *90*(1), 87–104.

Foulger, G., Julian, B., Hill, D., Pitt, A., Malin, P., & Shalev, E. (2004). Non-double-couple microearthquakes at long valley caldera, california, provide evidence for hydraulic fracturing. *Journal of Volcanology and Geothermal Research*, *132*(1), 45–71.

Gudmundsson, M. T., Jónsdóttir, K., Hooper, A., Holohan, E. P., Halldórsson, S. A., Ófeigsson, B. G., ... others (2016). Gradual caldera collapse at bárdarbunga volcano, iceland, regulated by lateral magma outflow. *Science*, *353*(6296), aaf8988.

Harrington, R. M., & Brodsky, E. E. (2007). Volcanic hybrid earthquakes that are brittle-failure events. *Geophysical Research Letters*, *34*(6).

Holtzman, B., Groebner, N., Sawi, T., Xing, T., Pec, M., Ghaffari, H., ... others (2021). Unsupervised spectral feature extraction applied to acoustic emissions during brittle creep of basalt under dry and wet conditions. In *Agu fall meeting abstracts* (Vol. 2021, pp. H12E–04).

Holtzman, B., Paté, A., Paisley, J., Waldhauser, F., & Repetto, D. (2018). Machine learning reveals cyclic changes in seismic source spectra in geysers geothermal field. *Science advances*, *4*(5), eaao2929.

Jenkins, W. F., Gerstoft, P., Bianco, M. J., & Bromirski, P. D. (2021). Unsupervised deep clustering of seismic data: Monitoring the ross ice shelf, antarctica. *Journal of Geophysical Research: Solid Earth*, *126*(9), e2021JB021716.

Kelley, D. S., Delaney, J. R., & Juniper, S. K. (2014). Establishing a new era of submarine volcanic observatories: Cabling axial seamount and the endeavour segment of the juan de fuca ridge. *Marine Geology*, *352*, 426–450.

Lomax, A., Michelini, A., Curtis, A., & Meyers, R. (2009). Earthquake location, direct, global-search methods. *Encyclopedia of complexity and systems science*, *5*, 2449–2473.

Lomax, A., Virieux, J., Volant, P., & Berge-Thierry, C. (2000). Probabilistic earthquake location in 3d and layered models: Introduction of a metropolis-gibbs method and comparison with linear locations. *Advances in seismic event location*, 101–134.

Nooner, S. L., & Chadwick, W. (2016). Inflation-predictable behavior and co-eruption deformation at axial seamount. *Science*, *354*(6318), 1399–1403.

Sawi, T., Holtzman, B., Walter, F., & Paisley, J. (2022). An unsupervised machine-learning approach to understanding seismicity at an alpine glacier. *Journal of Geophysical Research: Earth Surface*, e2022JF006909.

Sawi, T., Waldhauser, F., Holtzman, B. K., & Groebner, N. (2023). Detecting repeating earthquakes on the san andreas fault with unsupervised machine learning of spectrograms. *The Seismic Record*, *3*(4), 376–384.

Schaff, D. P., & Waldhauser, F. (2005). Waveform cross-correlation-based differential travel-time measurements at the northern california seismic network. *Bulletin of the Seismological Society of America*, *95*(6), 2446–2461.

Scholz, C. H., Tan, Y. J., & Albino, F. (2019). The mechanism of tidal triggering of earthquakes at mid-ocean ridges. *Nature communications*, *10*(1), 2526.

Seydoux, L., Balestriero, R., Poli, P., Hoop, M. d., Campillo, M., & Baraniuk, R. (2020). Clustering earthquake signals and background noises in continuous seismic data with unsupervised deep learning. *Nature communications*, *11*(1), 3972.

Song, Z., Tan, Y. J., & Roman, D. C. (2023). Deep long-period earthquakes at akutan volcano from 2005 to 2017 better track magma influxes compared to volcano-tectonic earthquakes. *Geophysical Research Letters*, *50*(10), e2022GL101987.

Tan, Y. J., Waldhauser, F., Tolstoy, M., & Wilcock, W. S. (2019). Axial seamount: Periodic tidal loading reveals stress dependence of the earthquake size distribution (b value). *Earth and Planetary Science Letters*, *512*, 39–45.

Tolstoy, M., Vernon, F. L., Orcutt, J. A., & Wyatt, F. K. (2002). Breathing of the seafloor: Tidal correlations of seismicity at axial volcano. *Geology*, *30*(6), 503–506.

Waldhauser, F., & Ellsworth, W. L. (2000). A double-difference earthquake location algorithm: Method and application to the northern hayward fault, california. *Bulletin of the seismological society of America*, *90*(6), 1353–1368.

Waldhauser, F., Wilcock, W., Tolstoy, M., Baillard, C., Tan, Y., & Schaff, D. (2020). Precision seismic monitoring and analysis at axial seamount using a real-time double-difference system. *Journal of Geophysical Research: Solid Earth*, *125*(5), e2019JB018796.

White, R., & McCausland, W. (2016). Volcano-tectonic earthquakes: A new tool for estimating intrusive volumes and forecasting eruptions. *Journal of Volcanology and Geothermal Research*, *309*, 139–155.

Wilcock, W. S., Dziak, R. P., Tolstoy, M., Chadwick Jr, W. W., Nooner, S. L., Bohnenstiehl, D. R., ... others (2018). The recent volcanic history of axial seamount: Geophysical insights into past eruption dynamics with an eye toward enhanced observations of future eruptions. *Oceanography*, *31*(1), 114–123.

Wilcock, W. S., Tolstoy, M., Waldhauser, F., Garcia, C., Tan, Y. J., Bohnenstiehl, D. R., ... Mann, M. E. (2016). Seismic constraints on caldera dynamics from the 2015 axial seamount eruption. *Science*, *354*(6318), 1395–1399.

Wilding, J. D., Zhu, W., Ross, Z. E., & Jackson, J. M. (2023). The magmatic web beneath hawai ‘i. *Science*, *379*(6631), 462–468.

Woods, J., Donaldson, C., White, R. S., Caudron, C., Brandsdóttir, B., Hudson,

T. S., & Ágústsdóttir, T. (2018). Long-period seismicity reveals magma pathways above a laterally propagating dyke during the 2014–15 bárarbunga rifting event, iceland. *Earth and Planetary Science Letters*, *490*, 216–229.

Yoon, C. E., O'Reilly, O., Bergen, K. J., & Beroza, G. C. (2015). Earthquake detection through computationally efficient similarity search. *Science advances*, *1*(11), e1501057.

Yu, H., Harrington, R. M., Kao, H., Liu, Y., & Wang, B. (2021). Fluid-injection-induced earthquakes characterized by hybrid-frequency waveforms manifest the transition from aseismic to seismic slip. *Nature communications*, *12*(1), 6862.

Zhu, W., & Beroza, G. C. (2019). Phasenet: a deep-neural-network-based seismic arrival-time picking method. *Geophysical Journal International*, *216*(1), 261–273.

Zhu, W., McBrearty, I. W., Mousavi, S. M., Ellsworth, W. L., & Beroza, G. C. (2022). Earthquake phase association using a bayesian gaussian mixture model. *Journal of Geophysical Research: Solid Earth*, *127*(5), e2021JB023249.